

Ultra-coherent meta-emitter tailors arbitrary thermal wavefront

Received: 15 September 2025

Accepted: 26 January 2026

Published online: 31 January 2026

 Check for updates

Rui Chen^{1,2}, Tianle Chen¹, Mengqi Liu³, Xingsi Liu³, Sen Zhang¹, Faizan Raza¹, Hongguang Dong¹, Yongdi Dang¹, Zejie Yu¹, Huan Hu², Jianbing Xu⁴, Cheng-Wei Qiu^{3,5}✉ & Yungui Ma¹✉

Conventional coherent light-field manipulation techniques inherently conflict with the spatiotemporal incoherence of thermal radiation sources. While recent advances in thermophotonics have facilitated directional thermal emission, arbitrary thermal wavefront control—a cornerstone for advanced functionalities like focusing and holography—remains an unaddressed challenge. Here, we report a generalized recipe of designing meta-emitters with lossy and lossless outer boundaries, that enables thermal emission with arbitrarily tailored wavefront. Lossy and lossless surfaces on two sides of the meta-emitter are synergistically coupled by a single-mode waveguide, transforming incoherent thermal photons to coherent surface waves for wavefront shaping functionalities. Designer surface mode of meta-emitter permits the independent optimization of photon lifetime and propagation length, thus enabling scalable spatial coherence engineering. For the proof of concept, we experimentally demonstrate near-diffraction-limited self-focusing emission, quasi-two-dimensional (quasi-2D) high-quality thermal holography without speckle noise and spatial-multiplexed holography. Coupling optimization further suggests that spatial coherence exceeding $1000\lambda_0$ are achievable. Our proposed meta-emitter establishes a paradigm-shifting framework to integrate stochastic thermodynamic emission with precision photonic engineering, opening avenues for information-rich thermal radiation technologies.

As a ubiquitous physical phenomenon rooted in fundamental thermodynamics, thermal radiation inherently generates broad-spectrum electromagnetic (EM) waves governed by Planck's law¹. While its applications span from primitive illumination to a variety of modern technologies such as infrared detection² and passive cooling³, conventional implementations predominantly manipulate photon intensity within the diffusive regime. The inherent spatiotemporal incoherence and polarization randomness of thermal photons set an

insurmountable barrier for their integration into phase-critical photonic systems—a realm exclusively served by coherent laser sources. Although bulk optical configurations incorporating spectral filters and polarization modulators can partially enhance thermal light correlation, such approaches inevitably introduce prohibitive energy losses and system complexity⁴. This persistent challenge underscores the critical scientific question: how to engineer compact thermal emitters that directly generate wavefront-engineered coherent radiation?

¹State Key Lab of Modern Optical Instrumentation, Centre for Optical and Electromagnetic Research, International Research Center for Advanced Photonics, College of Optical Science and Engineering, Zhejiang University, Hangzhou, Zhejiang, China. ²Zhejiang University-University of Illinois Urbana-Champaign Institute (ZJU-UIUC Institute), Zhejiang University, Haining, Zhejiang, China. ³Department of Electrical and Computer Engineering, National University of Singapore, Singapore, Singapore. ⁴Department of Electronic Engineering, Materials Science and Technology Research Centre, The Chinese University of Hong Kong, Hong Kong SAR, China. ⁵Nanotech Energy and Environment Platform, National University of Singapore Suzhou Research Institute, Suzhou, Jiangsu, China. ✉ e-mail: chengwei.qiu@nus.edu.sg; yungui@zju.edu.cn

Resolving this conundrum holds transformative potential for bridging the gap between thermodynamic principles and photonic information technologies, representing an enduring pursuit in the scientific community over the past decades.

Enhancing thermal coherence necessitates simultaneous phase correlation improvement across both spectral and spatial domains. In 1990s, Greffet et al. discovered long-range near-field correlation can be achieved along the emission surface with the aid of resonant surface modes, such as surface-plasmon polaritons (SPPs) or surface-phonon polaritons (SPhPs)^{5,6}. In 2002, they pioneered the experiment to generate and observe this coherent thermal emission over a polar crystal (silicon carbide) surface⁷. Subsequent advances in metasurfaces spurred the development of resonant architectures—including SPhPs^{8–13}, SPPs^{14–18}, coupled resonant cavities¹⁹, bound states in the continuum (QBIC)^{4,20,21} and extended guided modes^{22–24}—enabling the

engineering of spatiotemporal coherence through tailored dispersion relations.

For these resonant absorptive surfaces, resonant modes rely on collective interactions across a large number of periodic units, rendering their resonant behavior highly sensitive to the structural variations. However, structural complexity is crucial for shaping wavefronts²⁵. While slightly introducing local perturbations can achieve asymmetric unidirectional emission²¹, band splitting introduces additional lattice modes that severely disrupt the emission wavefronts and degrade the signal-to-noise ratio (SNR), as illustrated in the left panel of Fig. 1a. Further increasing the structural complexity to an aperiodic arrangement necessitates multi-layered nano-fabrications to suppress the local perturbation to the nonlocal resonances, which hinder its experimental developments⁴. Besides, long range of disorder leads to a higher density of split subbands, approaching a quasi-

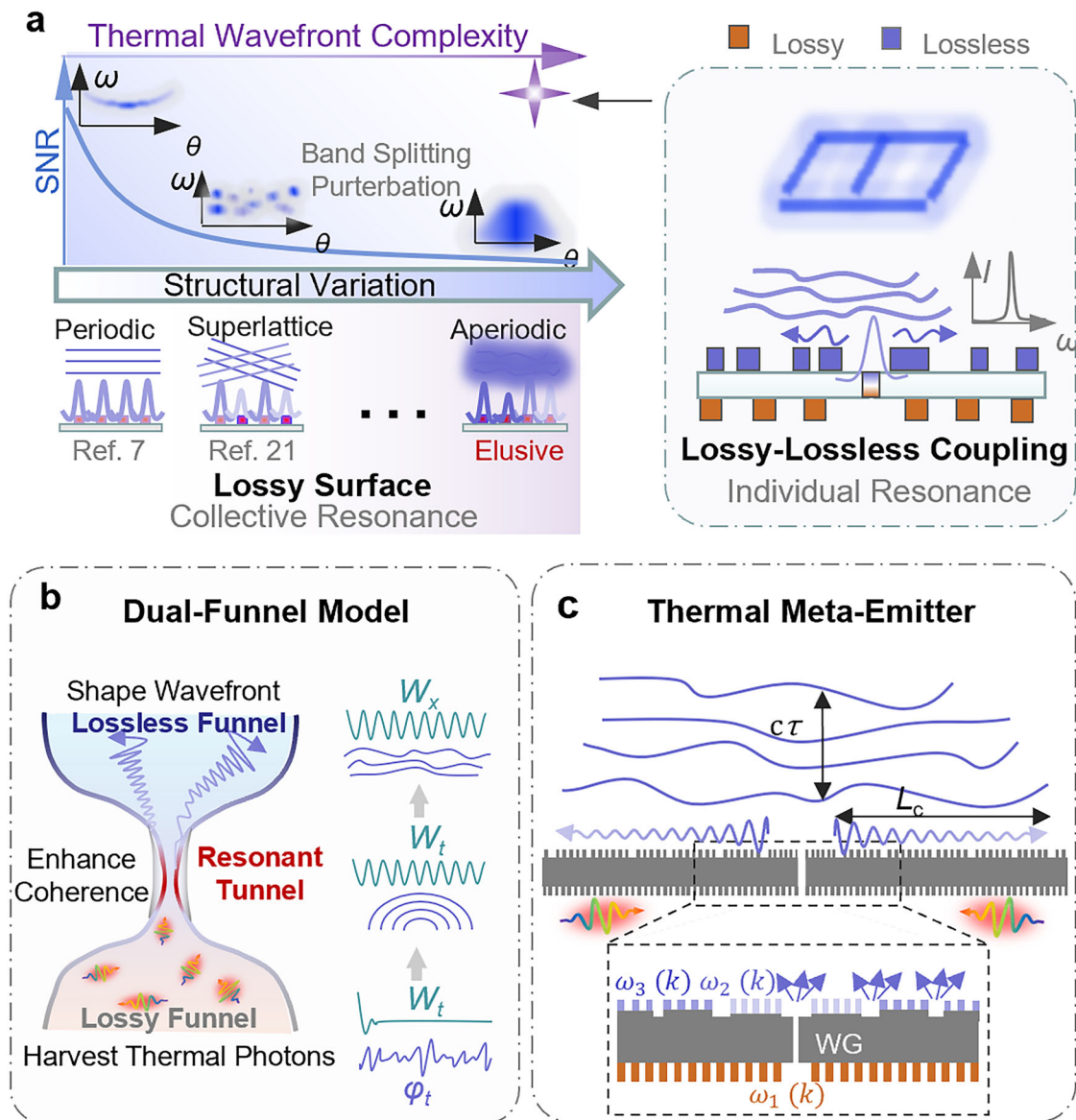


Fig. 1 | The challenge of thermal wavefront modulation and schematic of meta-emitter. a Challenges in thermal wavefront shaping. In the resonant lossy surface framework, an inherent trade-off exists between the signal-to-noise ratio (SNR) and the complexity of the thermal wavefront, rendering the emission of intricate thermal wavefronts elusive. In contrast, the lossy and lossless resonant coupling framework suppress the mutual perturbation between resonance and local scatterers, enabling complex thermal wavefront emission with high SNR. **b** Concept of

DF model. Thermal photons generated within the “lossy funnel” are transported to the “lossless funnel” through a bridging resonant “tunnel” while extending their lifetime. **c** Cross-section of the schematic architecture of DF meta-emitter. The inset enlarges the view of the DF meta-emitter around the central WG. Dispersion relationships $\omega(k)$ on both sides can be designed by various structures for specific wavefront control requirement. Temporal coherence: $c\tau$; local scatterer: S; WG: waveguide.

continuum band (see Supplementary Notes S1.2-1.3 for detailed analysis). This broadened band degrades the coherence of resonances, making it challenging to achieve complex thermal wavefront emission, such as thermal focusing and holography.

Separating the lossy resonance and lossless emitter could significantly suppress the local perturbations to the resonance, thereby theoretically enabling complex emission functionalities²⁶. However, their experimental realization faces challenges, such as position-dependent absorptive-structural fabrication and limited emission power. Due to these limitations, although extensive efforts have been made to enhance the coherence of the thermal radiation, all the experimental demonstrations so far have been confined to planar wavefront emission. More complex wavefront emissions, such as thermal focusing and holography, remain largely theoretical^{4,13,26}. Detailed emission performances and mechanism comparisons between our work and previous studies can be found in Supplementary Note S1.1 and Supplementary Table 1.

Here, we introduce a thermal meta-emitter incorporating separating but synergistic waveguide-coupled lossy and lossless boundaries, enabling arbitrary thermal wavefront manipulation capability without sacrificing SNR or too much emission power, as shown in Fig. 1a. The single connecting waveguide ensures fixed scattering phase relationship on the scattering surface, endowing meta-emitters with arbitrary phase modulation capability. Experimentally, we demonstrate self-focusing thermal emission with near-diffraction-limit performance and quasi-2D high-quality coherent thermal holography with negligible speckle noise, providing the first experimental demonstration of deterministic thermal wavefront control that approaches monochromatic-level performance metrics. Furthermore, we show that the proposed framework can be spatially encoded to realize multiplexed thermal holography. By optimizing the connecting resonance, the spatial coherence of our device can be further extended to $100\lambda_0$ while retaining all these fascinating functionalities (asymmetric emission, focusing and holography). This work establishes a paradigm-shifting platform for coherent thermal radiation control, enabling functional wavefront shaping capabilities that bridge the gap between thermodynamic emission and precision photonic engineering.

Results

Architecture of meta-emitter

The meta-emitter incorporates near-field synergistically coupled lossy and lossless boundaries, which can be aptly conceptualized as a dual-funnel (DF) model, as schematically shown in Fig. 1b. Similar to conventional thermal metasurfaces, the bottom ‘lossy funnel’ engineers the thermally populated electromagnetic mode, and transports it to the ‘lossless funnel’ through a coupling resonant ‘tunnel’ while extending their lifetime. These long lifetime photons correlate the scatterers in the ‘lossless funnel’ with designed phase-delay, thereby efficiently enabling the transformation of the temporal coherence (W_t) to the spatial coherence (W_x) of tailored emission waves. The connecting tunnel serves as an effective coherent source, fixing the scattering phase on the lossless funnel, similar to the point source in ref. 26. The thickness of the design can be suppressed to λ_0 , which is similar to that of conventional thermal metasurfaces.

The corresponding physical architecture is shown in Fig. 1c, comprising two corrugated metallic surfaces with an inner bridging waveguide (WG) tunnel at the center. In this bull’s eye configuration^{27–30}, thermally populated photons from the lossy bottom surface are efficiently transported to the lossless top surface for devising manipulation, driven by the strong Fabry-Pérot (FP) resonance occurring inside the central WG tunnel. Besides, this narrow WG tunnel effectively mitigates the dispersion-induced ‘rainbow effect’ prevalent in periodic structures^{7,14,31}. The cavity mode’s quality factor (Q -factor) dictates the temporal coherence of transmitted thermal photons, which is transformed into the spatial coherence through the

propagation of surface modes. Local scatterers on this radiation surface can be strategically introduced as defect perturbations to contrive phase-correlated thermal emission.

Different from the previous studies usually utilizing band edge standing wave modes with a large Q -factor to enhance spatial coherence, our architecture decouples resonator and scatterers to fully leverage propagating surface wave to efficiently transform the temporal coherence into spatial coherence. The spatial coherence L of meta-emitter characterizes the distance traveled by the wave packet accumulating a specific phase-delay difference, which can be linked to the temporal coherence via the relation $\Delta\phi = L\Delta\beta = \tau\Delta\omega$, where $\Delta\beta$ and τ are respectively the wavevector difference within $\Delta\omega$ and the photon lifetime. For a high Q resonance ($\Delta\omega \rightarrow 0$) with a specific mode lifetime, the spatial coherence can be expressed by the function of mode lifetime as $L \approx \tau \frac{d\omega}{d\beta} = \tau \cdot v_g$, where v_g denotes the group velocity. Supplementary Note S2 showcases an example of the two surface modes with similar lifetime at the same operational frequency could have obviously different spatial coherences along the surface. For the bandedge mode, the band variance can no longer be reflected by the group velocity; the higher-order polynomial expansion term, such as band curvature ($b \propto d^2\omega/d\beta^2$), needs to be applied^{4,21,32} to estimate the spatial coherence.

Physically, this conclusion can be understood as the distance traveled by wave packet within its lifetime. It’s worthy to note that, temporal coherence (Q -factor of the mode) just set an upper boundary of spatial coherence ($L_c = c\tau$, where c is the light speed in free space), different spatial coherence can be obtained with the same temporal coherence by modifying the slope of the operational band, which is not clarified in the previous studies.

Leveraging this temporal-to-spatial coherence transformation concept, we employ spoof SPPs in our study as energy carriers owing to their low-loss and band-engineerable characteristics across the entire thermal spectrum spanning from terahertz to mid-infrared frequencies. Critically, groove-geometries enabled radiation phase and group velocity manipulation capability makes it easily meet the versatile requirements for complex thermal wavefront shaping. Figure 2a plots the band diagrams of three representative spoof SPP modes explored in our design: a nonradiative bounded mode (BM) below the light cone and two radiative modes: a weakly radiative mode (W-RM) and a strongly radiative mode (S-RM). The W-RM can be viewed as a perturbed version of the BM, where enlarging one of the grooves within a long period folds the band into the light cone. The S-RM represents the extreme case of the W-RM, obtained by removing all the interconnection grooves within the period. The band diagrams of three modes with light lines are shown in Supplementary Fig. 5. The plasma frequency follows the relation $\omega_{\text{spoof}} = \pi c/2h$ (where c is the light velocity in vacuum), allowing for broadband adaptability through freely adjustable groove depth h ^{33,34}. As shown in Fig. 2b, with realistic material loss, the surface mode lifetime τ_{surf} (defined as $\tau_{\text{surf}} = Q_{\text{surf}}/\omega_0$) and decay length L_D (calculated as: $L_D = \tau_{\text{surf}} \cdot v_g$) of spoof SPPs can vary in two orders of magnitude, providing the flexibility in accommodating devices in different dimensional scales.

When the propagation loss is small, the spatial coherence of thermal photons is mainly influenced by the finite lifetime τ_{WG} of WG mode, which determines the bandwidth (Fig. 2c, inset). This WG mode exhibits a dynamic balance between radiative dissipation and intrinsic damping losses. As shown in Fig. 2c, τ_{WG} (Q -factor, $\tau_{\text{WG}} = Q_{\text{WG}}/\omega_0$) peaks at $\tau_{\text{WG,max}} = 25\tau_0$ with $\tau_0 = 2\pi/\omega_0$ for optimal WG width w_1 , confirming the geometric configuration that minimizes loss. Our theoretical framework (Discussion and Supplementary Note S14) predicts that advanced tunneling cavity designs could suppress loss channels, potentially enhancing $\tau_{\text{WG,max}}$ by two orders of magnitude. The energy transfer efficiency from bottom surface mode to the radiation interface achieves resonant amplification, showing a significant enhancement at matched frequencies compared to off-resonance states

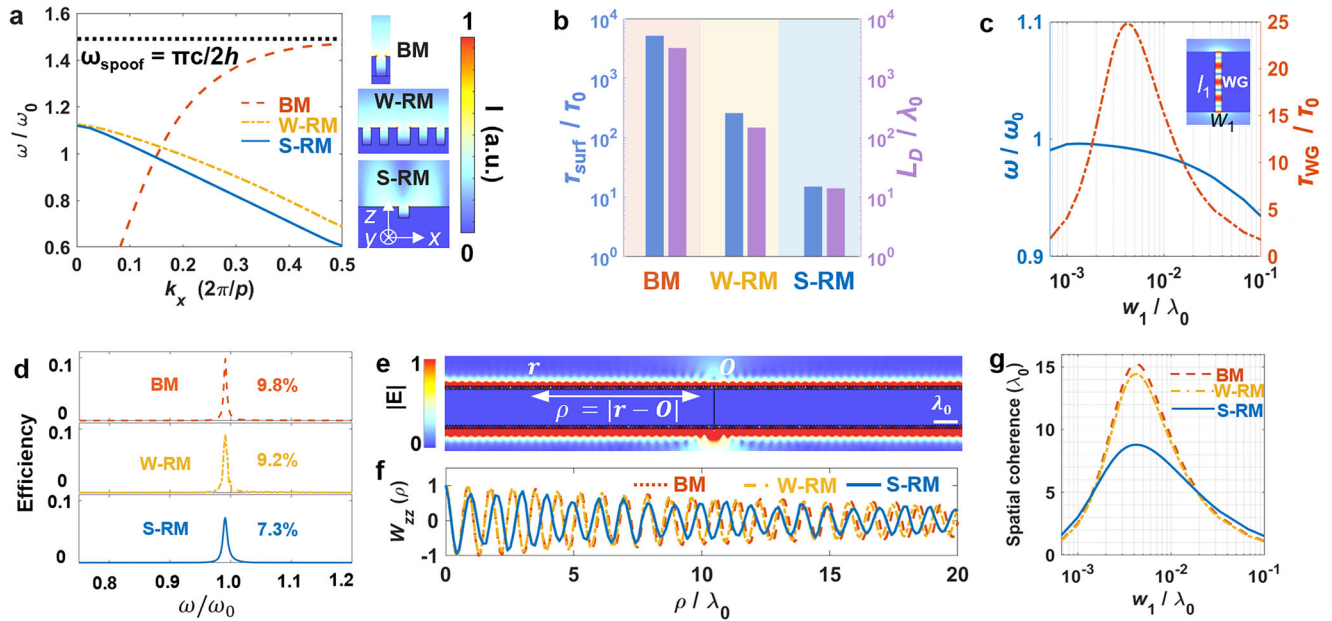


Fig. 2 | Design and characteristics of meta-emitter. **a** Dispersion diagrams of different spoof SPP modes. The periods of the BM, W-RM and S-RM are $0.13\lambda_0$, $0.70\lambda_0$ and $0.87\lambda_0$, respectively. Groove widths and depths are $0.06\lambda_0$ and $0.13\lambda_0$ for BM, $0.1\lambda_0$ and $0.11\lambda_0$ for S-RM. For W-RM, the width of center groove is the same as that in S-RM and other parameters are the same as those in BM. Mode profiles of single unit at frequency ω_0 are shown in the right panel. **b** The mode lifetime ($\tau_{\text{surf}} = Q/\omega$, $\tau_0 = 2\pi/\omega_0$, blue bars) and propagation length ($L_D = \tau_{\text{surf}} v_g$, $v_g = \frac{d\omega}{dk}$ at ω_0) along the surface (purple bars) for the above modes. The y-axis is normalized by λ_0 . **c** The eigenfrequency and mode lifetime as a function of

w_1 . $l_1 = 2\lambda_0$ is set in the simulation. Inset: the eigenmode profile. **d** Energy tunneling efficiencies of the hybrid mode with BM on the bottom surface and BM, W-RM and S-RM on the top surface. $l_1 = 2\lambda_0$, $w_1 = \lambda_0/150$ are set in the simulation. **e** Eigenmode profile of the meta-emitter. The BM is configured as both the bottom and top structures in the simulation. Here, O and r represent the coordinates of the WG and an arbitrary point on the top surface, while ρ denotes the distance between these two points. **f** Cross-spectral density component $W_{zz}(\rho)$ of the surface wave as a function of ρ at fixed height $z_0 = \lambda_0/10$ above the surface. **g** Spatial coherence of different surfaces as a function of w_1 .

(Fig. 2d). This phenomenon arises from near-field coupling between confined surface waves and the WG cavity mode, as visualized by their superimposed electric field distributions (Fig. 2e). The hybrid modes create a photonic “superhighway” that preferentially channels thermal energy while suppressing parasitic dissipation. The lifetime of the hybrid mode is governed by the reciprocal relation $1/\tau = 1/\tau_{\text{WG}} + 1/\tau_{\text{surf}}$. Detailed efficiency simulations and comparisons between our design and classical giant transmission schemes^{27,28,35} are provided in Supplementary Note S3.1. By applying an additional metal board to transform the surface waveguide into a photonic crystal, the bottom surface can be designed as a defect cavity, boosting the emissivity of the device to ~75%. The corresponding design strategies and discussion are also provided in Supplementary Note S3.2.

Crucially, our DF architecture enables independent modulation of these critical parameters. Figure 2g illustrates the spatial coherence of three modes (BM, W-RM, S-RM) as a function of the geometric parameter w_1 at the operational frequency ω_0 . The WG mode’s finite lifetime fundamentally limits coherence, with measured maxima of $15\lambda_0$, $14\lambda_0$ and $9\lambda_0$ for BM, W-RM, and S-RM, respectively. This discrepancy highlights propagation loss effects under high- Q bridging cavity conditions. For validation, cross-spectral density analysis by the component^{36,37} $W_{zz}(\rho, z = \lambda_0/10) = \langle E_z^*(O, z)E_z(\rho, z) \rangle$ was also performed in simulated data, as plotted in Fig. 2f. The $l_1/\sqrt{\epsilon}$ correlation lengths of the W_{zz} are $14\lambda_0$, $13\lambda_0$ and $8\lambda_0$ for BM, W-RM and S-RM, respectively, consistent with the monochromatic model predictions, laying the foundation for the further wavefront manipulation. Detailed derivations are provided in the Method section.

In the following, advanced coherent devices can be obtained through the rational design of local defect scatterers on the emission surface. Due to the narrow width of the designed scatterers (around $\lambda_0/10$), the emitted phase can be simplified to solely depend on the propagation phase of the spoof SPPs^{38,39}. To streamline the

experimental implementation and analysis, our experiments are conducted in the terahertz regime where wavelength-scale phenomena permit precise defect engineering and near-field characterization.

Self-focusing thermal emission

Our first application is to demonstrate diffraction-limited self-focusing thermal emission using a one-dimensional (1D) meta-emitter. As schematically depicted in Fig. 3a, the self-focusing device features a hybrid mode design. The bottom surface is engineered to operate in S-RM, enabling efficient harvesting of ambient thermal energy. Meanwhile, the top surface functions in W-RM and is divided into two distinct functional zones: an outer radiative region (S_r) and an inner coupling region (S_c). Grooves in the coupling region are optimized to match momentum with the WG mode, whereas those in the radiative region are engineered to operate in W-RM. Here, local scatterers are strategically introduced to fulfil the desired emission wavefront. For focusing functionality, it will satisfy a spherical spatial phase profile, i.e.,

$$\varphi(x) = k_0 \cdot (\sqrt{x^2 + f^2} - f) \tag{1}$$

where x is the coordinate on the surface, f is the focal length and k_0 is the free-space wavevector. The position of scatterers is determined by the condition of $\varphi(x) + k_{\text{spp}}x = 2m\pi$, where m is an integer and k_{spp} is the wavevector of spoof SPP optimized for radiative grooves. Details on parametric optimizations, including k_{spp} , groove dimensions, and S_c functionality, are provided in Supplementary Note S4 and Supplementary Table 2. For the optimized structure, the eigenmode field analysis (Fig. 3b) reveals a well-defined focusing pattern with a focal length $f = 10\lambda_0$ ($\lambda_0 \approx 3$ mm) and numerical aperture N.A. = 0.7. It achieves a high focusing efficiency of ~95% (defined as the ratio of the integrated energy at the focal line to the energy at the WG exit, details

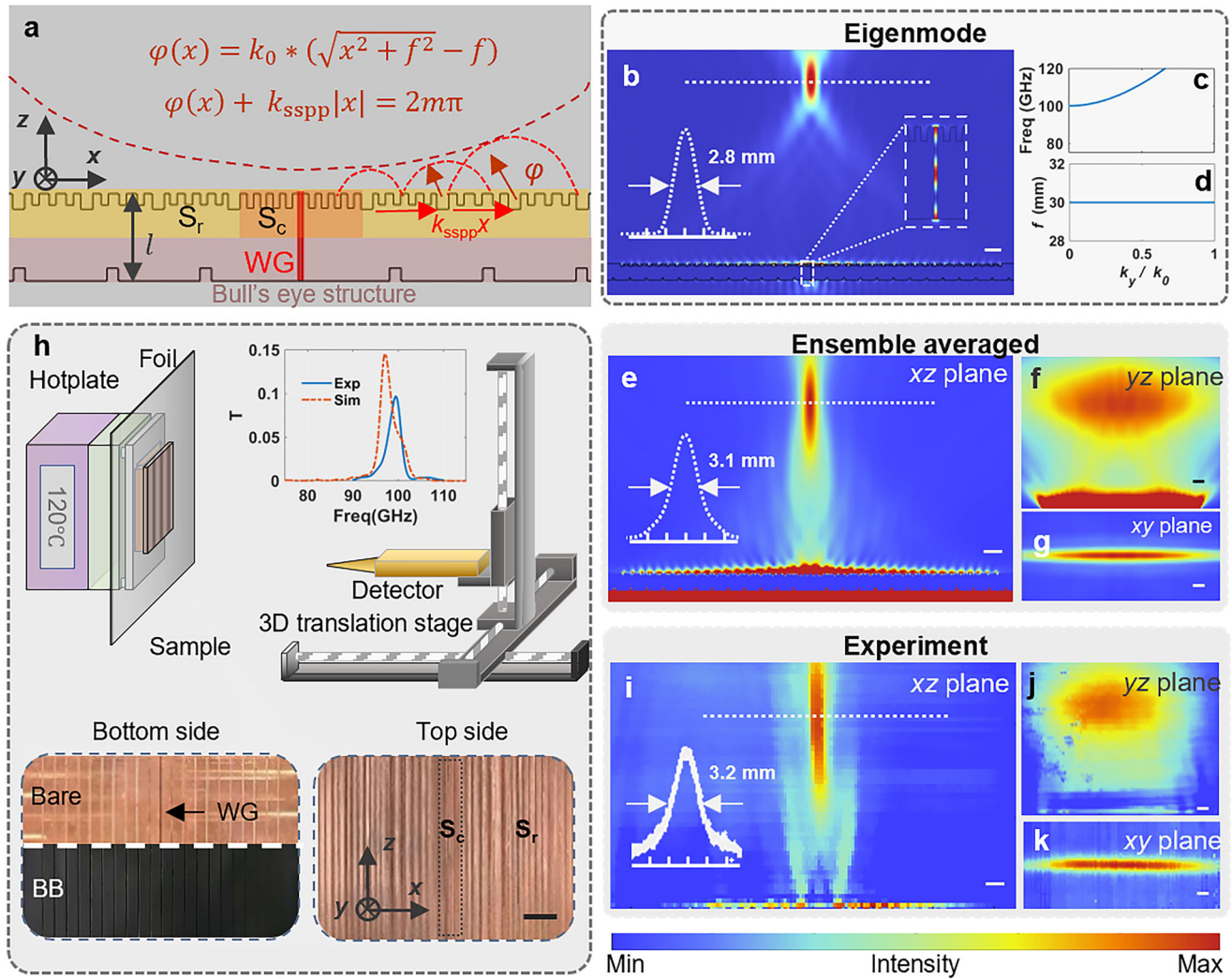


Fig. 3 | Self-focusing thermal meta-emitter. **a** The surface wave modulation design. S_c denotes the coupling surface region, which couples the output energy from the WG to the spoof SPPs. S_r represents the radiation surface region, where spoof SPPs are scattered at designed positions to form a focusing profile. **b** Eigenmode profile of the designed structure. The inset shows an enlarged view of the white dashed region, with the intensity rescaled to clearly display the WG mode pattern. Copper with conductivity of $\sigma = 5.8 \times 10^7$ S/m is applied in the simulation. **c** Out-of-plane wavevector (k_y) dispersion of the meta-emitter. **d** Focal length of eigenmode as a function of k_y . The WG length is set to 2.9 mm in the simulation. **e–g** Ensemble-averaged intensity profiles in the xz , yz , and xy planes under random dipole excitation. **h** Schematic of the experimental setup. The sample coated with a blackbody layer on the back side is heated using a hot plate. The thermal radiation

pattern is collected point by point using a millimeter-wave detector mounted on a 3D translation stage. A foil-wrapped board is employed to block background thermal noise from the hot plate. Upper inset: simulated and measured transmission spectrum of the sample under plane wave excitation at normal incidence. Bottom insets: photographs of the sample images on both sides. Bare and black-body painted bottom surfaces are presented in the upper panel and bottom panel in the inset. WG: waveguide. The temperature is maintained at 120 °C during the measurement. **i–k** Measured intensity profile at xz , yz , and xy plane, respectively. Scalar bar: 3 mm. The detailed comparison of intensity profiles in the experiment and simulation can be found in Supplementary Note S9 and Supplementary Fig. 19. Fig. **b**, **e**, and **i** show focal intensity cross-sections in their insets, with FWHM marked on the profiles.

can be found in the Supplementary Note S4 and Supplementary Fig. 10) and a tightly confined focal line of $0.93\lambda_0$ (equivalent N.A. = 0.53) realized under the incidence of nonuniform surface wave across the aperture. The focal line width can be further reduced to the ideal limit of $0.72\lambda_0$ by engineering the radiative loss of the top surface to achieve a near-uniform scattered amplitude wavefront at the expense of dissipating surface wave energy at the edge of the device. A comprehensive time-domain analysis in Supplementary Note S5 elucidates the transient focusing process initiated by a dipole source positioned near the bottom surface. Supplementary Movie 1 vividly exhibits the dynamic evolution of the hybrid coupling of the spoof SPPs with WG mode, significantly extending the lifetime of thermal photons. In addition, it is important to note that although the FP modes in the central WG exhibit dispersion with respect to the transverse wavevector k_y , as shown in Fig. 3c (detailed information can

be found in Supplementary Note S6), the leaky groove-based metasens employed here features the desired achromatic focusing property (Fig. 3d). Photons of different frequencies converge to form a transverse focal line at the common focal plane $z=f$, which boost energy utilization efficiency.

To numerically characterize the stochastic thermal emission behavior of our design, we performed 100 simulations with randomly distributed dipole excitation below the bottom surface with distance of $0.3\lambda_0$ to obtain statistical results (detailed simulation methods given in “Method”²⁶). Averaged intensity profiles across different planes (Fig. 3e–g) demonstrate robust focusing performance: the obtained full-width-at-half-maximum (FWHM) ($1.03\lambda_0$) of the ensemble-averaged focal line closely approaches the diffraction limit ($0.93\lambda_0$) observed in eigenmode simulations (Fig. 3b), confirming high spatial coherence across the entire aperture. The slightly broader FWHM in

the ensemble-averaged case relative to the eigenmode result (inset, Fig. 3b) arises from contributions of off-resonant frequencies near the eigenfrequency. This effect can be further mitigated by enhancing the Q -factor of the WG mode, such as tunnel geometry optimization analyzed in the Discussion part.

With the optimized design, a copper sample was fabricated using the computer numerical control (CNC) cutting technique. The transmission spectrum under normal incidence (inset, Fig. 3h) shows good agreement with simulations, though the measured transmission peak is slightly broader and blue-shifted, primarily due to fabrication tolerances. The groove fabrication tolerances are within the sculpturing precision of state-of-art CNC techniques. A weak absorptive layer, ~ 60 μm blackbody paint (BB paint Musou black 2.0, $n \approx 1 + 0.02i$ @100 GHz), was applied to the bottom surface for thermal photon generation, as shown in the inset of Fig. 3h. This BB layer has minor influence on the lifetime and decay length for S-RM mode in the design, due to its weak localization property. The detailed analysis on the lifetime and decay length degradation for surface modes caused by BB layer is presented in the Supplementary Note S7. The detailed fabrication tolerance analysis is presented in Supplementary Note S8.

The thermal measurement setup and sample photographs are presented in Fig. 3h. The detailed experimental information is given in the Methods section. Using this setup, intensity profiles at different planes were mapped, as shown in Fig. 3i–k. The intensity mapping validation is analyzed in Supplementary Note S9. The FWHM of the measured focal line is ~ 3.2 mm ($1.06\lambda_0$), closely matching the statistical numerical result ($1.03\lambda_0$) plotted in Fig. 3e. Importantly, the near-diffraction-limit focusing performance indicates that all grooves contribute coherently to the focal spot, with a spatial coherence equivalent to the aperture size ($11\lambda_0$)—almost an order of magnitude longer than the state-of-the-art reported in ref.²¹. Other measurements align well with simulations, including intensity distributions in xz and yz planes, as quantitatively compared in Supplementary Fig. 19c–e. The intensity local minima near the center WG is originated from the non-ideal interference of the waves scattered from the left and right sides of lens grooves, due to the depth fabrication error in the coupling region around the slit exit. The detailed analysis can be found in Supplementary Note S8.4.

The flat-topped focal line profile arises from the detector's finite response band (75–120 GHz), which attenuates high-frequency components with large transverse wavevector k_y , which is analyzed in Supplementary Note S10 by ray-tracing calculation. Detailed experimental methodologies are given in the Methods section.

Polarization and spatial multiplexed coherent thermal holography

In this section, we demonstrate 1D and quasi-2D coherent thermal holography with more complex light-field manipulation using our DF meta-emitter architecture. Leveraging the design flexibility of S-RM, we introduce polarization multiplexing along orthogonal directions. The shallow grooves ($< \lambda_0/5$) together with low filling ratio ($< 10\%$, defined as groove width w to the period p , $F = w/p$) of S-RM, ensuring that the cross-polarization-coupling between orthogonal channels can be neglected. By integrating these advantages with a scattering-based holographic design approach^{39–41}, we experimentally realize quasi-2D coherent thermal holography through superposition of patterns with distinct polarization states, as exemplified by the digital “8” in Fig. 4a–d. Higher-order diffraction observed in Fig. 4b, d—attributed to fabrication tolerances—can be minimized using precision nanofabrication techniques. Non-uniform background noise arising from detector zero-point drift is addressable via advanced methods like lock-in amplification^{42,43}. Experimental results for additional holographic numbers (0, 4, 7) are shown in Fig. 4e–g, all achievable through the proposed design framework. To quantitatively evaluate the quality of holographic image⁴⁴, we calculate the $\text{SNR} = \langle I \rangle / s$, in which $\langle I \rangle$ and s

are the mean and standard deviation of intensity within the blue rectangle box marked in Fig. 4f. Moderate coherence of the engineered thermal light greatly suppresses the speckle noise⁴⁵, leading to a high image quality ($\text{SNR} = 22$). Detailed design schematics and polarization multiplexing strategies are provided in Supplementary Note S11.

To further showcase the wavefront control versatility of our design, we develop and experimentally realize a spatially multiplexed holographic device, as depicted in Fig. 4h. Grooves within the central shadowed region of the top surface are optimized to simultaneously accommodate two distinct holographic wavefront profiles (Fig. 4i). By leveraging the directional propagation of spoof SPPs along the radiative surface, two unique emission states are achieved through selective excitation of corresponding WGs. Experimental switching between blocked WGs yields separate holographic patterns of ‘5’ and ‘2’ (Fig. 4j–k), with the activated excitation slit WG indicated below each image. Detailed optimization procedures and structural parameters are provided in Supplementary Note S12. Additionally, adjusting the WG width enables tuning of emitted wave coherence: off-axis focusing with multiple diffraction orders demonstrates low coherence, while spatially multiplexed designs with insufficient mode decay highlight excessive spoof SPP spatial coherence (Supplementary Note S13). This demonstration of polarization and spatial multiplexing in thermal holography underscores the design's feasibility and adaptability for complex wavefront engineering.

Discussion

For our meta-emitter, the spatial coherence is primarily governed by the lifetime of the WG mode, which is fundamentally limited by metallic wall losses (Supplementary Fig. 30a). Through strategic slot geometry optimization—particularly elongating the central WG region—we achieve a 4000-fold enhancement in photon lifetime by enlarging the mode volume, thereby extending spatial coherence to $1000\lambda_0$ (Supplementary Note S14, Fig. 30b–g). This loss suppression strategy effectively redistributes electromagnetic energy density away from lossy interfaces. Limited by the computational capability, highly directional oblique emission, near diffraction-limited thermal self-focusing and holography devices with $100\lambda_0$ spatial coherence are demonstrated in Supplementary Note S14 and Supplementary Fig. 31–35. Furthermore, coherence can be systematically enhanced by engineering the surface mode's band structure (steep dispersion gradients) and loss characteristics. Tailoring these parameters enables selective suppression of decoherence channels while preserving hybrid mode coupling efficiency.

Beyond 1D and quasi-2D thermal wavefront engineering demonstrated above, our meta-emitter platform can also be extended to perform true 2D thermal wavefront shaping. By applying BM with axially symmetric bull's eye structure on the bottom surface with holographic pattern generation techniques on the top surface, sophisticated emission wavefronts (such as holography, vortex beam) can be obtained^{39,40}. One example of focused radially polarized thermal beam is designed in Supplementary Note S15. The polarization distribution of the focal spot shows good radial polarization property, as shown in Supplementary Fig. S36c–d. While the central hole in the bull's-eye structure imposes strict transmission constraints, optimizing coupling between bottom-surface spoof SPPs and the hole cavity—combined with critical balancing of radiative and absorption losses—significantly enhances device transmission and overall efficiency.

The top surface, engineered primarily for far-field wavefront control, can also be tailored to manipulate surface wave profiles^{46,47}, enabling applications in on-chip photonic systems. Although the current surface-wave-mediated emission is restricted to p -polarized modes, integrating Pancharatnam-Berry (PB) meta-atoms could extend functionality to arbitrary polarization states^{46,48}. Beyond the terahertz, millimeter-wave, and microwave regimes discussed herein, our SPP-based design strategy could scale naturally to far- and mid-

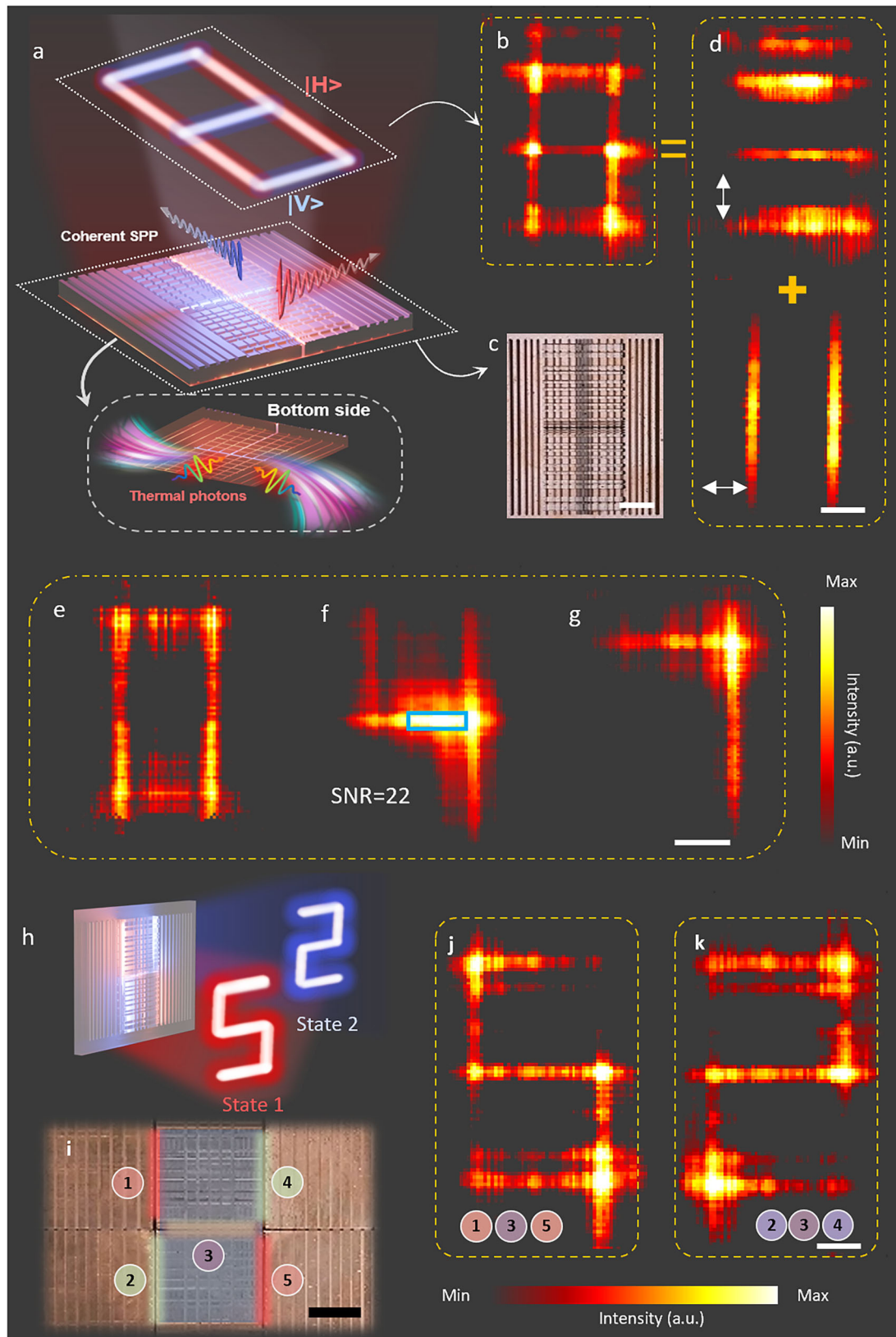


Fig. 4 | Measurement of coherent thermal hologram. **a** Schematic diagram of the hologram of “8”. **b, c** Holographic pattern and image of the top side of sample. **d** The intensity distribution of y -polarized, x -polarized light. **e–g** Holographic patterns for “0”, “4” and “7”, respectively. **h** Schematic diagram of spatial multiplexed holography. By exciting different grooves, two holographic states can be switched. **i** Image of the top side of the spatial multiplexed sample. 5 slits with sequential

numbers (1–5) are marked in the figure. Red (1, 3, 5) and blue (2, 3, 4) lines denote the excitation WGs for the hologram of ‘5’ and ‘2’, respectively. The shadow region in the center denotes the spatial multiplexed area. **j, k** Holographic patterns for ‘5’ and ‘2’, respectively. Corresponding excitation WG numbers are marked below. Scalar bar: 1 cm.

infrared wavelengths—critical for room-temperature thermal radiation studies. The increased absorption loss can be mitigated by employing low-confinement surface mode, such as S-RM mode in Fig. 2a, and compensated by further reducing the size of the radiative perturbations. Supplementary Note S16 demonstrates this scalability with a self-focusing emission device operating at 5.7 μm , achieving single-mode property in a wide band (2–10 μm) and near-diffraction-limited (FWHM $\approx 3.6 \mu\text{m}$) focusing performance. The high aspect ratio (>10) of metallic slit and double-sided metal sculpture can be accomplished by the state-of-the-art nano-fabrication and alignment techniques.

In conclusion, we present a straightforward and robust meta-emitter to realize coherent thermal emission with customized wavefronts. Experimental validations, including self-focusing emission and thermal holography in the millimeter-wave band, confirm the efficacy of our design. Beyond serving as a physical demonstration of thermal wavefront engineering, the capability of generating highly coherent light with tailored wavefronts carries substantial practical significance. This innovative approach may pave the way for compact transmitters in next-generation (6 G) communications or mid-infrared anti-counterfeiting displays, promoting system miniaturization and fostering advancements in these domains. We envision that the current work will catalyze the development of advanced thermal devices and unlock potential applications in green-energy communications and display technologies.

Methods

Simulation method of surface mode

The dispersion properties and mode profiles of BM, W-RM and S-RM in Fig. 2a are obtained through 2D simulations using the eigenfrequency solver in COMSOL Multiphysics. The material of the metal is set as copper ($\sigma = 5.8 \times 10^7 \text{ S/m}$) in the simulation. The propagation lengths along the surface for each mode in Fig. 2b are calculated from the Q factors and wavevectors of modes at their designed frequencies. The Q factor indicates how quickly the mode loses energy during one cycle of oscillation and can be directly reflected in the lifetime of the mode:

$$\tau = Q/\omega \quad (2)$$

where ω_0 is the angular frequency of the resonance.

The lifetime τ characterizes the decay property in the time domain, defined as the time of the mode energy decay to $1/e$ of its original value. For its counterpart, the propagation length of the spoof SPPs reveals the spatial distances over which the mode energy decays to $1/e$ of its original value, which can be expressed as

$$L = v_g \cdot \tau \quad (3)$$

where v_g is the group speed of spoof SPP along the surface, given by

$$v_g = d\omega/d\beta \quad (4)$$

Substituting for v_g and τ , we can rewrite the expression for L as:

$$L = \frac{d\omega}{d\beta} \cdot Q/\omega \quad (5)$$

where Q factor and $d\omega/d\beta$ can be obtained from simulation.

The eigenfrequency, Q factor, and eigenmode profile shown in Fig. 2c are obtained by eigenfrequency study in COMSOL Multiphysics. Perfect Matched layers are set as all the boundaries.

The spatial coherence of the entire device presented in Fig. 2g is calculated by the propagation length of the hybrid mode of slit mode and surface mode on the top side. The Q factor of the hybrid mode can

be obtained by:

$$Q_{\text{hybrid}} = (Q_{\text{surf}}^{-1} + Q_{\text{WG}}^{-1})^{-1} \quad (6)$$

Then, the spatial coherence can be obtained by the Equation 5.

Calculation of the cross-spectral density component W_{zz}

To characterize the spatial coherence of the spoof SPPs on the top surface, we calculated the cross-spectral density component of W_{zz} for the electric field of spoof SPPs (E_z) above the surface at $z = \lambda_0/10$, with $\lambda_0 = 3 \text{ mm}$. The E_z field distribution is obtained by performing 2D frequency domain simulation in COMSOL Multiphysics software. Perfectly matched layers are set as the boundary in the simulation. To attain the E_z fields at different frequencies, an electric dipole with a frequency range from 75–120 GHz is set as the source to excite the spoof SPPs on the bottom side. Three types of top surfaces are simulated. The space-frequency dependent real parts of E_z components are drawn in Supplementary Fig. 5a–c, respectively.

The slit resonance determines the frequency-dependent part, and the same slit results in similar sharp peaks for all the surface modes. The spatial dependence of E_z reflects the energy attenuation of surface modes across the surface, which corresponds to the propagation lengths of modes shown in Fig. 2b. For S-RM, the short propagation length ($\sim 10\lambda_0$) leads to obvious attenuation in E_z , as illustrated in Supplementary Fig. 5a. In contrast, the strong EM wave confinement capability of BM and W-RM enables them to exhibit a negligible attenuation of E_z within the range of $20\lambda_0$, Supplementary Fig. 5c. Cross-correlation function of E_z for these three modes at a different spatial interval of ρ can be expressed as^{36,37}:

$$w_{zz} \left(\rho, z = \frac{\lambda_0}{10}, \omega \right) = E_z^*(O, z, \omega) E_z(\rho, z, \omega) \quad (7)$$

as shown in Supplementary Fig. 5d–f. The spatial attenuation behavior of E_z drawn in Supplementary Fig. 5a–c can also be reflected in the cross-correlation function at each frequency. By taking the ensemble average of w_{zz} , cross-spectral density component $W_{zz} = \langle w_{zz} \rangle_\omega$ is obtained as described in the main text.

Simulation of the thermal self-focusing performance

We employ Ansys Lumerical FDTD Solutions for the 3D simulation of the entire design. An electric dipole with a random phase, orientation angle, and x, y coordinates is placed on the bottom surface ($0.3\lambda_0$ away from the bottom surface) as the source to capture the intensity profiles at different frequencies for each plane. This simulation is repeated 100 times, each with a different random dipole source. The average of all simulated intensity profiles is then calculated to obtain the statistical emission profiles for each plane, as shown in Fig. 3e–g. In the simulations, the emission intensities of all random dipoles are set identically. The transmitted energy obtained from each dipole simulation is shown in Supplementary Fig. 11, where the differences originate from the varying coupling efficiencies between individual random dipoles and the bottom surface mode. This excitation-efficiency variation reflects the fundamental process by which thermally populated surface waves are generated, namely that dipoles with near-normal surface polarization possess higher excitation efficiency. Such coupling-induced transmittance fluctuations do not affect the coherence enhancement performance of the designed resonant tunnel.

Measurement and characterization

To characterize the transmission property of the fabricated sample, a vector network analyzer (VNA) with horn antenna is applied. The transmission spectrum in Fig. 3h is measured under normal incidence.

For the thermal measurement, the sample painted with a black-body on the bottom side is heated by a hot plate. A 5 mm thick metal

spacer is precisely positioned between the sample and the hot plate using thermally conductive adhesive to maintain a fixed separation distance. A foil-wrapped board is applied to block background thermal noise from the hot plate. The thermal radiation pattern generated by the sample on the top side is measured by a polarization-dependent detector on a translation stage point by point. To improve the accuracy of the mapping measurement, a waveguide probe with a sharp tip is designed for the detector. The detailed information of probe design can be found in Supplementary Note S9.

Data availability

All the data in this study are provided within the paper and its supplementary information.

Code availability

All the code that supports the findings of this study is available from the corresponding author upon request.

References

- Planck, M. Ueber das Gesetz der Energieverteilung im Normalspectrum. *Ann. Phys.* **309**, 553–563 (1901).
- Bao, F. et al. Heat-assisted detection and ranging. *Nature* **619**, 743–748 (2023).
- Zhai, Y. et al. Scalable-manufactured randomized glass-polymer hybrid metamaterial for daytime radiative cooling. *Science* **355**, 1062–1066 (2017).
- Overvig, A. C., Mann, S. A. & Alù, A. Thermal metasurfaces: complete emission control by combining local and nonlocal light-matter interactions. *Phys. Rev. X* **11**, 021050 (2021).
- Carminati, R. & Greffet, J.-J. Near-field effects in spatial coherence of thermal sources. *Phys. Rev. Lett.* **82**, 1660–1663 (1999).
- Le Gall, J., Olivier, M. & Greffet, J.-J. Experimental and theoretical study of reflection and coherent thermal emission by a SiC grating supporting a surface-phonon polariton. *Phys. Rev. B* **55**, 10105–10114 (1997).
- Greffet, J.-J. et al. Coherent emission of light by thermal sources. *Nature* **416**, 61–64 (2002).
- Caldwell, J. D. et al. Low-loss, infrared and terahertz nanophotonics using surface phonon polaritons. *Nanophotonics* **4**, 44–68 (2015).
- Lu, G. et al. Engineering the spectral and spatial dispersion of thermal emission via polariton–phonon strong coupling. *Nano Lett.* **21**, 1831–1838 (2021).
- Wang, T. et al. Phonon-polaritonic bowtie nanoantennas: controlling infrared thermal radiation at the nanoscale. *ACS Photonics* **4**, 1753–1760 (2017).
- Ma, B. et al. Narrowband diffuse thermal emitter based on surface phonon polaritons. *Nanophotonics* **11**, 4115–4122 (2022).
- Arnold, C. et al. Coherent thermal infrared emission by two-dimensional silicon carbide gratings. *Phys. Rev. B* **86**, 035316 (2012).
- Chalabi, H., Alù, A. & Brongersma, M. L. Focused thermal emission from a nanostructured SiC surface. *Phys. Rev. B* **94**, 094307 (2016).
- Park, J. H., Han, S. E., Nagpal, P. & Norris, D. J. Observation of thermal beaming from tungsten and molybdenum bull’s eyes. *ACS Photonics* **3**, 494–500 (2016).
- Han, S. E. & Norris, D. J. Beaming thermal emission from hot metallic bull’s eyes. *Opt. Express* **18**, 4829–4837 (2010).
- Lochbaum, A. et al. Compact mid-infrared gas sensing enabled by an all-metamaterial design. *Nano Lett.* **20**, 4169–4176 (2020).
- Wang, X. et al. Observation of nonvanishing optical helicity in thermal radiation from symmetry-broken metasurfaces. *Sci. Adv.* **9**, eade4203 (2023).
- Laroche, M. et al. Highly directional radiation generated by a tungsten thermal source. *Opt. Lett.* **30**, 2623 (2005).
- Dahan, N. et al. Enhanced coherency of thermal emission: Beyond the limitation imposed by delocalized surface waves. *Phys. Rev. B* **76**, 045427 (2007).
- Wang, K. et al. High-Q resonance engineering in momentum space for highly coherent and rainbow-free thermal emission. *Nano Lett.* **25**, 3613–3619 (2025).
- Nolen, J. R., Overvig, A. C., Cotrufo, M. & Alù, A. Local control of polarization and geometric phase in thermal metasurfaces. *Nat. Nanotechnol.* **19**, 1627–1634 (2024).
- Sun, K., Levy, U. & Han, Z. Exploiting zone-folding induced quasi-bound modes to achieve highly coherent thermal emissions. *Nano Lett.* **24**, 764–769 (2023).
- Sun, K., Cai, Y., Huang, L. & Han, Z. Ultra-narrowband and rainbow-free mid-infrared thermal emitters enabled by a flat band design in distorted photonic lattices. *Nat. Commun.* **15**, 4019 (2024).
- Sun, K., Yang, B., Cai, Y., Kivshar, Y. & Han, Z. Circularly polarized thermal emission driven by chiral flatbands in monoclinic metasurfaces. *Sci. Adv.* **11**, eadw0986 (2025).
- Cui, T.-J., Liu, S. & Li, L.-L. Information entropy of coding metasurface. *Light Sci. Appl.* **5**, e16172 (2016).
- Zhou, M. et al. Self-focused thermal emission and holography realized by mesoscopic thermal emitters. *ACS Photonics* **8**, 497–504 (2021).
- Lezec, H. J. et al. Beaming light from a subwavelength aperture. *Science* **297**, 820–822 (2002).
- Genet, C. & Ebbesen, T. W. Light in tiny holes. *Nature* **445**, 39–46 (2007).
- Martín-Moreno, L., García-Vidal, F. J., Lezec, H. J., Degiron, A. & Ebbesen, T. W. Theory of highly directional emission from a single subwavelength aperture surrounded by surface corrugations. *Phys. Rev. Lett.* **90**, 167401 (2003).
- García-Vidal, F. J., Martín-Moreno, L., Lezec, H. J. & Ebbesen, T. W. Focusing light with a single subwavelength aperture flanked by surface corrugations. *Appl. Phys. Lett.* **83**, 4500–4502 (2003).
- Baranov, D. G. et al. Nanophotonic engineering of far-field thermal emitters. *Nat. Mater.* **18**, 920–930 (2019).
- Overvig, A., Mann, S. A. & Alù, A. Spatio-temporal coupled mode theory for nonlocal metasurfaces. *Light Sci. Appl.* **13**, 28 (2024).
- Pendry, J. B., Martín-Moreno, L. & García-Vidal, F. J. Mimicking surface plasmons with structured surfaces. *Science* **305**, 847–848 (2004).
- Yu, N. et al. Designer spoof surface plasmon structures collimate terahertz laser beams. *Nat. Mater.* **9**, 730–735 (2010).
- Janssen, O. T. A., Urbach, H. P. & T. & Hooft, G. W. Giant optical transmission of a subwavelength slit optimized using the magnetic field phase. *Phys. Rev. Lett.* **99**, 043902 (2007).
- Chen, Y. Optical coherence and electromagnetic surface waves. *Prog. Opt.* **65**, 105–172 (2020).
- Wolf, E. *Introduction to the Theory of Coherence and Polarization of Light*. (Cambridge University Press, 2007).
- Tetienne, J.-P. et al. Dipolar modeling and experimental demonstration of multi-beam plasmonic collimators. *N. J. Phys.* **13**, 053057 (2011).
- Chen, Y.-H., Huang, L., Gan, L. & Li, Z.-Y. Wavefront shaping of infrared light through a subwavelength hole. *Light Sci. Appl.* **1**, e26–e26 (2012).
- Komisar, D. et al. Multiple channelling single-photon emission with scattering holography designed metasurfaces. *Nat. Commun.* **14**, 6253 (2023).
- Liu, X. et al. Off-normal polarized single-photon emission with anisotropic holography metasurfaces. *Nano Lett.* **24**, 13867–13873 (2024).
- Li, C. et al. Near-field and far-field thermal emission of an individual patch nanoantenna. *Phys. Rev. Lett.* **121**, 243901 (2018).

43. Wojszwyk, L. et al. An incandescent metasurface for quasimonochromatic polarized mid-wave infrared emission modulated beyond 10 MHz. *Nat. Commun.* **12**, 1492 (2021).
44. Zeng, Y. Metalasers with arbitrarily shaped wavefront. *Nature* **643**, 1240–1245 (2025).
45. Georges, M., Zhao, Y. & Vandenrijt, J.-F. Holography in the invisible. From the thermal infrared to the terahertz waves: outstanding applications and fundamental limits. *Light Adv. Manuf.* **2**, 1 (2022).
46. Wang, Z. et al. Excite spoof surface plasmons with tailored wavefronts using high-efficiency terahertz metasurfaces. *Adv. Sci.* **7**, 2000982 (2020).
47. Han, J. et al. Tailorable polarization-dependent directional coupling of surface plasmons. *Adv. Funct. Mater.* **32**, 211000 (2022).
48. Wang, Z. et al. Efficient generation of vectorial terahertz beams using surface-wave excited metasurfaces. *Opto-Electron. Sci.* **4**, 240024–240024 (2025).

Acknowledgements

M.-Y.G. acknowledged the financial support by the Joint Funds of the National Natural Science Foundation of China (U24A20313), National Natural Science Foundation of China (62475234 and 62075196), National Key Research and Development Program of China (2024YFA1012600), Natural Science Foundation of Zhejiang Province LDT23F05014F05, Leading Innovative and Entrepreneur Team Introduction Program of Zhejiang (2021R01001) and Fundamental Research Funds for the Central University (2021FZZX001-07). C.R. acknowledged the financial support by the National Natural Science Foundation of China (62405268) and Postdoctoral Fellowship Program of CPSF (GZC20232261). C.-W.Q. acknowledged the financial support by the Ministry of Education, Republic of Singapore (Grant No.: A-8002978-00-00, A-8002152-00-00 and A-8002458-00-00), the National Research Foundation, Singapore (NRF) under NRFs Medium Sized Centre: Singapore Hybrid-Integrated Next-Generation-Electronics (SHINE) Centre funding programme, and the Science and Technology Project of Jiangsu Province (Grant No. BZ2022056). J. B. X. acknowledged the support from AoE/P-701/20.

Author contributions

M.-Y.G. conceived the idea. C.-R., C.-T.L., Y.-Z.J., Z.-S., F. R., D.-H.G. and D.-Y.D. performed the experiments. C.-R. conducted all the calculations and simulations. C.-R., L.-M.Q., C.-W.Q., and M.-Y.G. analyzed the data and prepared the manuscript with assistance from L.-X.S. The project is

supervised by H.-H., X.-J.B., M.-Y.G., and C.-W.Q. All the authors contributed to the manuscript revision.

Competing interests

The authors declare no competing interests.

Additional information

Supplementary information The online version contains supplementary material available at <https://doi.org/10.1038/s41467-026-69088-7>.

Correspondence and requests for materials should be addressed to Cheng-Wei Qiu or Yungui Ma.

Peer review information *Nature Communications* thanks Michele Cotrufo, Zhanghua Han, Kaili Sun, and the other anonymous reviewer for their contribution to the peer review of this work. A peer review file is available.

Reprints and permissions information is available at <http://www.nature.com/reprints>

Publisher's note Springer Nature remains neutral with regard to jurisdictional claims in published maps and institutional affiliations.

Open Access This article is licensed under a Creative Commons Attribution-NonCommercial-NoDerivatives 4.0 International License, which permits any non-commercial use, sharing, distribution and reproduction in any medium or format, as long as you give appropriate credit to the original author(s) and the source, provide a link to the Creative Commons licence, and indicate if you modified the licensed material. You do not have permission under this licence to share adapted material derived from this article or parts of it. The images or other third party material in this article are included in the article's Creative Commons licence, unless indicated otherwise in a credit line to the material. If material is not included in the article's Creative Commons licence and your intended use is not permitted by statutory regulation or exceeds the permitted use, you will need to obtain permission directly from the copyright holder. To view a copy of this licence, visit <http://creativecommons.org/licenses/by-nc-nd/4.0/>.

© The Author(s) 2026